Available online at www.sciencedirect.com
SCIENCE DIRECT®
Combustion and Flame 143 (2005) 11–26
Combustion and Flame
www.elsevier.com/locate/combustflame

Development and application of a comprehensive soot model for 3D CFD reacting flow studies in a diesel engine

Sangjin Hong [a], Margaret S. Wooldridge [a,*], Hong G. Im [a], Dennis N. Assanis [a], Heinz Pitsch [b]

[a] *Mechanical Engineering Department, University of Michigan, Ann Arbor, MI 48109-2125, USA*
[b] *Department of Mechanical Engineering, Stanford University, Stanford, CA, USA*

Received 14 July 2004; received in revised form 2 March 2005; accepted 9 April 2005

Available online 1 August 2005

Abstract

A three-dimensional reacting flow modeling approach is presented for diesel engine studies that can be used for predictions of trends in soot emissions for a wide range of operating conditions. The modeling framework employs skeletal chemistry for *n*-heptane for ignition and combustion, and links acetylene chemistry to the soot nucleation process. The soot model is based on integration and modification of existing submodels for soot nucleation, agglomeration, oxidation, and surface growth. With the optimized modeling parameters, the simulations agree well with results of high-pressure shock tube studies of rich *n*-heptane mixtures, reproducing the trends for soot mass over a range of temperature and pressure conditions ($T = 1550$–2050 K, $P = 20$, 40, and 80 MPa). Engine simulation results for soot mass are in excellent agreement with diesel engine smoke number measurements over a range of injection timings ($-11°$ ATDC–$2.4°$ ATDC) and two exhaust gas recirculation levels (16 and 26–27%). The model results demonstrate that correct description of the soot formation, as well as the soot transport processes, is critical for achieving reliable predictive capabilities in engine simulations.

Keywords: Soot emissions modeling; Computational engine simulations

1. Introduction

Despite the highly competitive thermal efficiency of the direct-injection diesel engine, the perennial NO*x*-soot emissions trade-off challenges its compliance with ever more stringent emissions regulations. In order to improve our understanding of the pollutant formation and destruction mechanisms, and to meet the demand for rapid design and development turnaround, three-dimensional computational fluid dynamic (CFD) models of reacting flow in engines are seeing increasing use. Engine soot models have ranged in complexity from phenomenological to detailed physico-chemical models. NO*x* emissions are typically modeled using variants of the extended Zeldovich mechanism.

Among the empirical soot models, the two-step model of Hiroyasu and Kadota [1] and its variants [2–8] have been used in a number of engine studies owing to its simplicity of implementation in CFD codes. This model is based on two empirical rate

* Corresponding author. Fax: +1 734 647 3170.
E-mail address: mswool@umich.edu (M.S. Wooldridge).

0010-2180/$ – see front matter
doi:10.1016/j.combustflame.2005.04.007

Nomenclature

A	Preexponential factor in rate coefficient expression (units of cm^3, mol, s)
A_C	Correction factor for nucleation rate expression
$\dot{C}_k$	Coagulation rate for kth soot moment
d_m	Average soot diameter (nm)
D	Sum of the turbulent soot diffusivity and the velocity slip diffusivity (m^2/s)
E	Activation energy (kcal/mol)
$\dot{G}_k$	Growth rate for kth soot moment
$\dot{I}_k$	Nucleation rate for kth soot moment
k_X	Per-site rate coefficient (cm^3/site/mol/s)
m_{Csoot}	Soot mass (g)
$\bar{M}_k$	kth mean soot moment
n	Power of temperature in rate coefficient expression
$n(v,t)$	Soot particle-size distribution (a log-normal distribution is assumed)
n_i, n_j	Number densities of soot particles of volume (size) i or j per unit volume ($1/cm^3\ cm^3$)
N_0	Avogadro's number (1/mol)
R	Universal gas constant (kcal/mol/K)
S_i	Surface area of ith soot particle (cm^2)
$\dot{S}_k$	Source/sink term for the kth moment
t	Time (s)
T	Temperature (K)
v	Soot volume (cm^3)
v_i, v_k	Volume of soot particle of size i or k (cm^3)
v_g	Average soot volume (cm^3)
v_1	Volume of one carbon atom
$\vec{v}$	Flow velocity vector (m/s)
X	Species designation
$[X]$	Molar concentration of species X (mol/cm^3)

Greek symbols

α	Fraction of surface sites available
$\beta(v_i, v_j)$	Collision frequency between soot particles of volume (size) i and j (m^3/s)
χ_S	Number density of surface sites ($2.3 \times 10^{15}\ cm^{-2}$)
σ	Standard deviation
$\dot{\omega}$	Reaction rate (mol/cm^3)

equations, formation and oxidation, which are functions of the major reactant concentrations. The model does not take into account particle growth and soot dynamics, its prediction of soot formation is linked explicitly to fuel concentration, and rate coefficients used in the empirical reactions often have to be modified when engine geometry or operating conditions are changed. This approach limits the applicability of the model as a predictive design tool to conditions where the model has been previously validated.

Tesner et al. [9] introduced an improved class of models by postulating formation of an intermediate species responsible for particle nucleation. Surovikin [10] assumed that the formation and growth of radical nuclei and the formation and growth of soot particle nuclei are different stages of the same process, partially superimposed on one another, but that they occur through different mechanisms. Hence, the particle formation process is assumed to consist of three stages: (i) the formation of radical nuclei, (ii) the growth of the radical nuclei and their conversion upon reaching a critical diameter into nuclei with a physical surface, and (iii) the further growth of the nuclei and their transformation into carbon particles. The standard KIVA-3V [11] soot model is primarily based on that of Surovikin [10], while the oxidation of soot particles follows the procedure of Haynes and Wagner [12] with rate constants from Nagle and Strickland-Constable [13]. Following the framework of Tesner et al. [9], a number of other researchers have linked the intermediate species for particle nucleation to acetylene [14,15], while others have introduced a generic soot precursor radical [16,17]. Nevertheless, this class of models still considerably oversimplifies the gas-phase combustion chemistry and neglects particle dynamics.

At the other extreme, detailed, multistep chemical models of soot formation and oxidation have been developed for canonical systems such as laminar flames [18–22], counterflow diffusion flames [23–26], and turbulent diffusion flames [27]. Application of a modeling framework derived from these approaches has been attempted in a few closed-cycle engine simulations [28,29], including the work of Kitamura et al. [30]. However, the extensive use of existing, detailed kinetic models in multidimensional simulations is still cost prohibitive and quantitative agreement with experimental data remains a challenge. Therefore, there is strong motivation to develop a soot formation model for practical fuels that can capture the essential physico-chemical processes, yet is amenable to large-scale simulations.

In addition to the soot physical chemistry, it is recognized that soot transport can play a large role in the soot emissions from engines and combustors [31,32]. However, the sensitivity of particulate emis-

sions to the soot transport dynamics and the methods used to model soot transport are often not well documented.

Based on the needs identified above, the objective of the current work is to develop a model that includes the broad scope of the physical and chemical mechanisms important in soot processes and is sufficiently simplified such that the soot model can be integrated into KIVA simulations of diesel combustion. The modeling approach is based on integration and modification (as necessary) of existing submodels for soot nucleation, agglomeration, oxidation, and surface growth. In addition, when appropriate, the model should account for soot particle transport which is different from that of gas-phase species. A key goal of the modeling effort is accurate predictions of trends in soot emissions for a wide range of operating conditions. The results of well-controlled shock tube studies by Kellerer et al. [33] are therefore used to calibrate the model and to develop confidence in the predictive capabilities. In the following sections, the submodels are described, comparisons with the experimental results are presented, and the sensitivity of the soot model to the input parameters of the component submodels is investigated. The work concludes with a comparison of KIVA simulation results with experimental data obtained from diesel engine studies.

2. Modeling approach

The modeling approach adopted in this study is based on our previous work on soot emissions of natural gas engines [34,35], where various submodels are incorporated and modified as necessary to represent each of the physical and chemical mechanisms considered important in soot modeling for engine studies. The basic framework of the soot modeling is the moment method, which has been used previously [18,36] to describe soot properties with reasonable accuracy and computational costs. In the moment method, the evolution of the soot properties is determined by the first three moments representing the soot number density (M_0), soot volume fraction (M_1), and the deviation from the average volume (M_2), using a presumed particle-size distribution. Specifically, a log-normal size distribution,

$$n(v,t) = \frac{1}{3\sqrt{2\pi}\ln\sigma}\exp\left[-\frac{\ln^2(v/v_g)}{18\ln^2\sigma}\right]\frac{1}{v}, \tag{1}$$

is used in this study. In Eq. (1), n is the number density of soot particles of volume v (where spherical particles are assumed throughout this work), v_g is average particle volume, and the σ is the standard deviation of the volume distribution. The assumption of a log-normal size distribution for soot particles is supported by experimental observations in engine studies [12,37,38]. Note that because a particle-size distribution is assumed, higher moments need not be calculated and significant computational savings are realized.

With a presumed log-normal size distribution, the first three soot moments are sufficient to resolve the soot properties using the relations

$$\bar{M}_k = \bar{M}_0 v_g^k \exp\left(\frac{9}{2}k^2\ln^2\sigma\right), \tag{2}$$

$$v_g = \frac{\bar{M}_1^2}{\bar{M}_0^{3/2}\bar{M}_2^{1/2}}, \tag{3}$$

$$\ln^2\sigma = \frac{1}{9}\ln\left(\frac{\bar{M}_0\bar{M}_2}{\bar{M}_1^2}\right). \tag{4}$$

The transient features of the soot moments are determined via

$$\frac{\partial\bar{M}_0}{\partial t} = \dot{I}_0 - \dot{C}_0, \tag{5}$$

$$\frac{\partial\bar{M}_1}{\partial t} = \dot{I}_1 + \dot{G}_1, \tag{6}$$

$$\frac{\partial\bar{M}_2}{\partial t} = \dot{I}_2 + \dot{G}_2 + \dot{C}_2, \tag{7}$$

where $\dot{I}_k$ is the nucleation rate, $\dot{G}_k$ is the combined growth and oxidation rates, and $\dot{C}_k$ is the coagulation rate for the $k = 0$, 1, and 2 moments. The source and sink terms represented in Eqs. (1)–(3) are developed based on the detailed physical and chemical submodels for the soot processes. The submodels include (a) skeletal reaction chemistry to represent ignition, combustion, and the formation of soot precursor species; (b) nucleation of soot primary particles coupled to the reaction kinetics; (c) soot coagulation based on collision theory; (d) soot oxidation by O_2 and OH; and (e) soot surface growth using a modified HACA mechanism.

2.1. Reaction chemistry

Because diesel engine combustion is the system of interest in the current work, n-heptane chemistry is used as a surrogate fuel to model the ignition, combustion, and soot nucleation chemical kinetics. The reaction mechanism employed in this study is provided in Liu et al. [39]. The mechanism is a skeletal form of a detailed mechanism for n-heptane [40], which is similar to the skeletal mechanisms by Pitsch and Peters [41] and Bollig et al. [42]. Compared with these previous mechanisms, the new mechanism has been enhanced and updated with the kinetic rate data provided by Baulch et al. [43,44] and others. The mechanism has been validated by comparison with ignition delay times from shock-tube [45] and

rapid compression machine experiments [46] at various temperatures, pressures, and equivalence ratios; species measurements from lean and rich plug flow reactor (PFR) experiments [47]; temperature measurements from PFR experiments for various initial temperatures [48] at elevated pressure; and species measurements in an *n*-heptane/air counterflow diffusion flame experiment [49]. Most importantly for the present study, all the major species and the acetylene mass fraction for the latter experiments are well predicted. The validation studies are documented in more detail in Liu et al. [39].

2.2. Nucleation of soot primary particles

The nucleation of soot primary particles is considered the least well-understood step in the soot formation process [50]. Although a unique soot precursor has not been identified, many species, including acetylene (C_2H_2), polyacetylene, benzene, and polycyclic aromatic hydrocarbon (PAH), have been suggested as important in the nucleation of soot primary particles [19,36]. Frenklach and Wang [19] estimated soot nucleation rates using collision processes of higher PAH compounds, which are only formed in the presence of acetylene. The use of PAH as a soot precursor, however, requires a relatively large reaction mechanism, resulting in increased computational costs and possibly a larger degree of empiricism, if the supporting chemistry is unknown. Thus, an alternative approach that does not involve PAH compounds is sought. Among the other compounds suggested above, acetylene has been proposed as an essential species in soot formation [51] and it is believed to participate in the PAH growth [50]. Because acetylene is considered a primary contributor to soot nucleation and its detailed kinetics are well represented in the skeletal *n*-heptane mechanism described above, nucleation of soot monomers was symbolized by the reaction:

$$C_2H_2 \Rightarrow 2C_{soot} + H_2. \quad \text{(R1)}$$

Here, $2C_{soot}$ represents a soot monomer that is composed of two carbon atoms. In this work, the rate constant for (R1) is an empirical global rate constant for soot formation, which is discussed further below. Once the soot monomers are formed, it is assumed that they immediately consolidate to form soot primary particles. It is then necessary to determine the total number of carbon atoms that constitute the soot primary particle. After investigating the effect of the primary particle size on the overall soot model (discussed in Section 3), the soot primary particles were assumed to consist of 32 carbon atoms. Thus, 16 soot monomers are required to form one soot primary particle, which is formed instantaneously from the soot monomers. When less than 16 soot monomers are available (i.e., when the number of monomers is not evenly divisible by 16), the monomers are consolidated to form a smaller soot primary particle to preserve conservation of carbon atoms. The stipulation that the primary particle consists of 32 carbon atoms is based on the work by Appel et al. [22] where the primary soot particles are formed by the collision of two pyrenes consisting of 16 C atoms each.

The average diameter, d_m, of the soot primary particles was determined by calculating the combined mass of the 32 carbon atoms, using a soot density of $\rho_{soot} = 1.8$ g/cm^3 [18], and assuming that the 32 carbon atoms combine to form a spherical particle, namely

$$\frac{\pi d_m^3}{6} = \frac{m_{Csoot}}{\rho_{soot}}. \quad (8)$$

The form of the rate coefficient for reaction (R1) is based on the fundamental assumption that the rate of production of the soot primary particles follows the rate of production of the important gas-phase species—acetylene. The soot nucleation rate expression considered is that proposed by Leung et al. [52],

$$\dot{\omega}_{nucleation} = 1.0 \times 10^4 \exp\left[\frac{-21{,}100}{T}\right] \times [C_2H_2]\ [\text{mol/cm}^3], \quad (9)$$

which was developed to represent direct formation of soot primary particles from acetylene.

The nucleation rate is incorporated into the moment model via

$$\dot{I}_k = A_C v_1^k \dot{\omega}_{nucleation} N_0, \quad (10)$$

where A_C is a correction factor, v_1 is the specific volume of the soot primary particle raised to the power of the kth moment, and N_0 is Avogadro's number. The correction factor in Eq. (10) is adjusted to investigate the sensitivity of the overall soot model to the nucleation submodel and to optimize the overall soot model performance under benchmark experimental conditions. The correction factor is set at the fixed value determined in the benchmarking studies for all subsequent engine modeling studies. The sensitivity analysis, model benchmarking, and validation processes are discussed further below.

2.3. Surface growth and oxidation

The reaction mechanism used in the current study for soot growth by surface reaction and soot oxidation is shown in Table 1, which is taken from Kitamura et al. [30] with one modification. In this mechanism, the surface growth model is based on the HACA mechanism [18,36] with the addition of several reaction

Table 1
The soot surface growth and oxidation mechanism of Kitamura et al. [30] used in the current work

	Reaction	$k = A\exp(-E/RT)$	
		A ($\mathrm{cm^3/mol\,s}$)	E (kcal/mol)
G1f	$C_{soot}\text{-}H + H \rightarrow C_{soot}\bullet + H_2$	2.5×10^{14}	12.0
G1b	$C_{soot}\bullet + H_2 \rightarrow C_{soot}\text{-}H + H$	4.0×10^{11}	7.0
G2f	$C_{soot}\bullet + H \rightarrow C_{soot}\text{-}H$	2.2×10^{14}	–
G2b	$C_{soot}\text{-}H \rightarrow C_{soot}\bullet + H$	2.0×10^{17}	109.0
G3[a]	$C_{soot}\bullet \rightarrow C_2H_2 +$ products	3.0×10^{12}	62.0
G4f	$C_{soot}\bullet + C_2H_2 \rightarrow C_{soot}CHCH\bullet$	2.0×10^{12}	4.0
G4b	$C_{soot}CHCH\bullet \rightarrow C_{soot}\bullet + C_2H_2$	5.0×10^{13}	38.0
G5	$C_{soot}CHCH\bullet \rightarrow C_{soot}\text{-}H + H$	5.0×10^{10}	–
G6	$C_{soot}\bullet + O_2 \rightarrow$ products	2.2×10^{12}	7.5
G7	$C_{soot}CHCH\bullet + O_2 \rightarrow$ products	2.2×10^{10}	7.5
G8	$C_{soot}\text{-}H + OH \rightarrow$ products	Reaction probability = 0.13	

[a] The preexponential factor listed for reaction G3 has been reduced from the original expression provided in Kitamura et al. [30] by a factor of 0.01.

paths suggested by Colket and Hall [53]. The surface growth mechanism includes possible acetylene elimination from the soot radical (reaction G3) and separates the acetylene addition process into a reversible formation of the radical adduct (reactions G4f and G4b) and a cyclization reaction (reaction G5). The rates for soot oxidation by O_2 and OH are taken from Appel et al. [22] and Neoh et al. [54], respectively. The modification of the preexponential factor for reaction G3 is based on the results of the sensitivity and validation studies. Details are presented below.

The contributions of soot growth and oxidation to the soot moment equations are calculated using the reaction mechanism in Table 1, along with the expression

$$\dot{G}_k^X = \int_0^\infty v_i^k k_X [X] \alpha \chi_S S_i n_i \,\mathrm{d}v_i, \tag{11}$$

where k_X is the per-site rate coefficient, $[X]$ is the concentration of the gaseous species involved in the surface reactions, α is the fraction of surface sites available for reaction, χ_S is the number density of surface sites, S_i is the surface area of the ith soot particle, and n_i is the particle size distribution function defined by the log-normal size distribution.

2.4. Particle growth by coagulation

Soot particle growth by collision is modeled using Smoluchowski's equation [55],

$$\dot{C}_k = \int_0^\infty v_i^k \frac{1}{2} \int_0^{v_i} \beta(v_j, v_k) n_j n_k \,\mathrm{d}v_j \,\mathrm{d}v_i - \int_0^\infty v_i n_i \int_0^\infty \beta(v_j, v_i) n_j \,\mathrm{d}v_j \,\mathrm{d}v_i, \tag{12}$$

where $\beta(v_j, v_i)$ is the collision frequency between soot particles, n_i and n_j are the number densities of soot particles of volume (size) i and j, respectively, and v_i and v_j are the volumes of soot particles of size i and j, respectively. Soot exhausted from automotive engines is known to be in the transition region between the free molecular and the continuum regimes [12,17,55]. The coagulation rate in the transition regime is typically determined using an interpolation formula. Here we use a continuum mean approximation [56],

$$\dot{C}_k = \frac{\dot{C}_k^{\mathrm{g}} \dot{C}_k^{\mathrm{f}}}{\dot{C}_k^{\mathrm{g}} + \dot{C}_k^{\mathrm{f}}}, \tag{13}$$

where $\dot{C}_k$ is the coagulation rate for the kth soot moment and $\dot{C}_k^{\mathrm{f}}$ and $\dot{C}_k^{\mathrm{g}}$ represent the coagulation rates for the kth soot moment in the free molecular regime and the gas-slip regime, respectively. As dictated by the size of the soot particles, the collision frequency of the free molecular regime, β_{F}, and the gas-slip regime β_{G} [56] are determined using the following relations:

$$\beta_{\mathrm{F}}(v_i, v_j) = K_{\mathrm{F}} \left(\frac{1}{v_i} + \frac{1}{v_j} \right)^{0.5} \left(v_i^{1/3} + v_j^{1/3} \right)^2, \tag{14}$$

$$\beta_{\mathrm{G}}(v_i, v_j) = K_{\mathrm{G}} \left(v_i^{1/3} + v_j^{1/3} \right) \times \left(C(v_i) v_i^{-1/3} + C(v_j) v_j^{-1/3} \right). \tag{15}$$

In Eqs. (14) and (15), $K_{\mathrm{F}} = (3/4\pi)^{1/6} \sqrt{6 k_{\mathrm{B}} T/\rho}$, $K_{\mathrm{G}} = 2(k_{\mathrm{B}} T/3\mu)$, and $C(v) = 1 + 1.257\,\mathrm{Kn}$, where Kn is the Knudsen number.

2.5. Soot particle transport

Although soot transport does not play a role in the model optimization and validation studies presented in the next section, the soot particle transport has been

identified as a key component to accurate soot modeling in engine studies [34]. Therefore, a brief description of the representation of the soot particle transport is provided here. Additional details are provided in Hong [35]. The soot transport model is used in subsequent engine simulation tests discussed in a later section of this work.

When soot particles are in the transition regime between continuum and free molecular flow, additional soot transport equations are required due to the velocity slip between the soot particles and the gas medium. The soot particle transport equation is expressed as

$$\frac{\partial \bar{M}_k}{\partial t} + \vec{\nabla} \cdot \left(\vec{v}\bar{M}_k\right) = \vec{\nabla}\left(D\vec{\nabla}\bar{M}_k\right)\dot{\bar{S}}_k, \tag{16}$$

where $\bar{M}_k$ is the kth mean soot moment, $\vec{v}$ is the flow velocity vector, D is the sum of the turbulent soot diffusivity and the diffusivity due to velocity slip, and $\dot{\bar{S}}_k$ represents the various source and sink terms for the kth moment (e.g., nucleation, oxidation, etc.). The turbulent soot diffusivity depends on particle size and appropriate expressions for the free molecular and transition regimes are used [57]. Thermophoretic forces on the soot particles are included in the soot transport modeling via calculation of a thermophoretic velocity after the approach described by Hinds [55].

3. Model calibration

The following procedure was used to calibrate the soot model and to validate the model beyond the calibration conditions. The experimental results of the shock-tube study by Kellerer et al. [33] were used to optimize the soot model in terms of three key parameters: the correction factor, A_C, used in the nucleation model (Eq. (10)), the rate coefficient of the surface reaction G3 (Table 1), and the size of the primary soot particles. The optimization of these parameters was determined via a detailed sensitivity analysis of the soot model. Once the optimal values were determined, the parameters were fixed at these values for the remainder of the model validation and engine studies.

In the shock-tube study by Kellerer et al. [33], time histories of soot carbon yield (defined as the ratio of the total carbon present in the soot particles to the total carbon available in the mixture, C_{soot}/C_{total}), soot number density, and mean soot particle diameter were determined for rich n-heptane mixtures, highly dilute in argon. These time-resolved measurements are presented by Kellerer et al. for one set of experimental conditions ($P = 25$ MPa, $T = 1750$ K, $[C] = 7.89$ mol/m^3, and $\phi = 5$). As we found no other time-resolved soot data available in the literature for n-heptane, these conditions were used as the basis for optimizing the transient behavior of the soot model. The temperature dependence of the soot model was calibrated using the overall measurements of soot yield presented in the same work. The soot yield measurements were obtained at conditions 1.5 ms after the passage of the reflected shock wave and the results span the temperature range $T = 1600$–2000 K and three pressures (20, 40, and 80 MPa). For the temperature calibration of the soot model, only the results of the $P = 40$ MPa conditions were used. A description of the sensitivity analysis, calibration procedure, and validation results follows.

The soot model and the gas-phase reaction mechanism were implemented in a homogeneous explosion problem configuration for the model calibration and validation. The initial conditions for the mixture composition were matched to the experimental input data. Throughout the reaction progress, adiabatic conditions with constant volume were assumed.

After numerous parametric studies, it was found that the rate coefficient for the surface reaction G3, the size of the soot primary particles, and the nucleation rate correction factor A_C were the soot model characteristics that were both the most uncertain and exhibited the strongest influence on the soot modeling results at the calibration conditions. Although the sensitivity analysis showed that results of changing the values of these parameters are coupled, the effects of the rate of the surface growth reaction G3 exhibited the most dramatic influence on the temperature dependence of the soot yield.

Fig. 1 shows the results of changing the preexponential factor (A_{G3}) for reaction G3 for the temperature range 1300–2100 K. Physically, increasing the value for A_{G3} reduces soot surface growth for existing particles while simultaneously releasing acetylene which can be used to nucleate new primary soot particles. When the reaction was not included in the surface mechanism ($A_{G3} = 0$), the overall soot yield was significantly higher than the experimental data and the maximum soot yield was obtained at $T > 2200$ K. When the rate coefficient for G3 was set at the value provided by Kitamura et al. [30] ($A_{G3} = 3 \times 10^{14}$), the soot particles experienced such rapid elimination of C_2H_2 and corresponding loss of surface growth sites, that the overall soot yield was significantly lower than the experimental values. In addition, for $A_{G3} = 3 \times 10^{14}$, the maximum soot yield was obtained at a temperature lower than 1500 K. Based on the two limiting results and further parametric studies, it was found that reducing A_{G3} by a factor of 0.01 ($A_{G3} = 3 \times 10^{12}$) resulted in reasonable qualitative agreement with the experimental data in terms of temperature dependence and acceptable quantita-

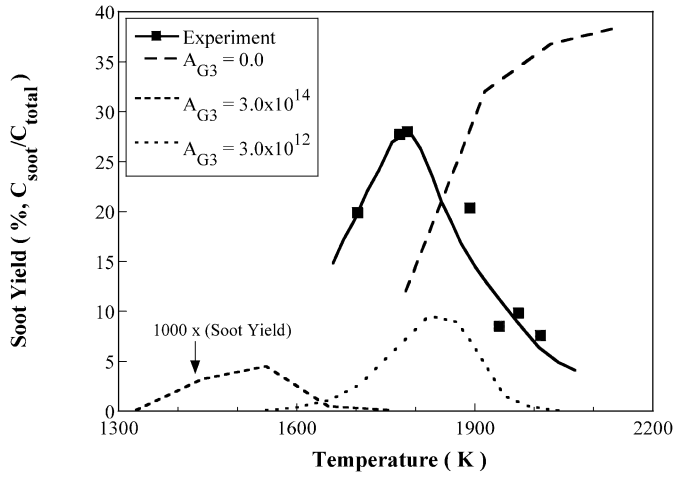

Fig. 1. The effect of the soot surface reaction G3 on soot yield as a function of temperature ($t = 1.5$ ms, $P = 4$ MPa, $A_C = 0.01$, and a primary soot particle size of 32C).

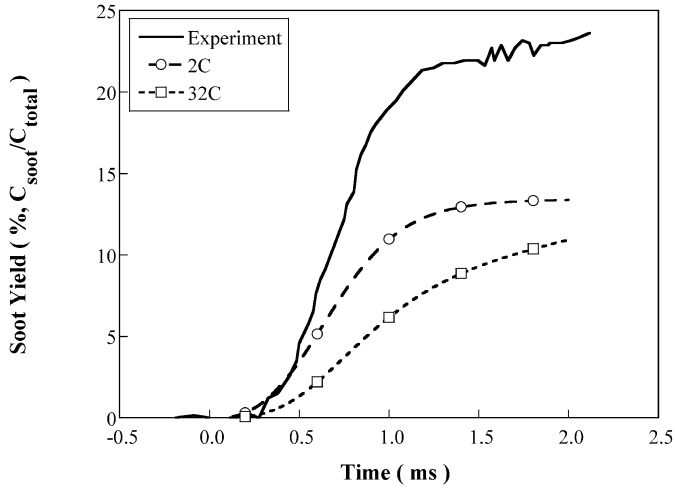

Fig. 2. Comparison of the experimental results of Kellerer et al. [33] and the modeling results ($A_{G3} = 3 \times 10^{12}$) of the present study for soot yield at conditions of $P = 2.5$ MPa, $T = 1750$ K, [C] $= 7.89$ mol/m^3, and $\phi = 5$. Sensitivity of the modeling results to the size of the primary soot particles is presented.

tive agreement in terms of the overall soot yield (see Fig. 1).

After the temperature dependence of the soot model was optimized for soot yield at 40 MPa, the effects of the size of the primary soot particles on the quantitative agreement with the soot yield, soot number density, and soot particle-size time histories were investigated. The results are presented in Figs. 2–4, showing a comparison of the experimental and predicted results for soot yield, average particle diameter, and soot number density as a function of time using the optimized value for A_C (discussed below) and k_{G3} for conditions of 25 MPa, 1750 K, [C] $= 7.89$ mol/m^3, and an equivalence ratio, $\phi = 5$. In the figures, $t = 0$ s represents the start of the simulation and the time when the reflected shock wave passes the measurement point in the experiments. Two primary soot particle sizes, 2C and 32C, were considered. Figs. 2–4 show that the predicted soot properties are in reasonable qualitative agreement with the experimental data, reproducing the transient response of the system quite well. The model results also indicate there is a trade-off among the quantitative agreement among the soot yield, the soot particle diameter, and the number density. For smaller primary soot particles (2C), fewer soot monomers are required to form a primary soot particle. Consequently, for an equivalent number of monomers, the soot number density for the 2C model is larger than that for the 32C model (see Fig. 4). Relative to the 32C model,

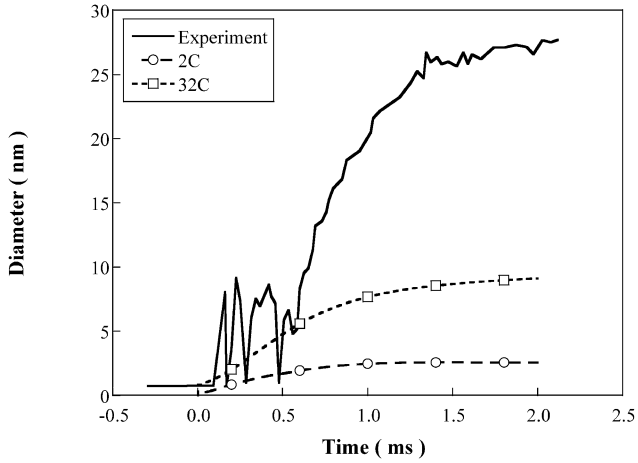

Fig. 3. Comparison of the experimental results of Kellerer et al. [33] and the modeling results of the present study for average soot particle diameter corresponding to the experimental and simulation conditions of Fig. 2.

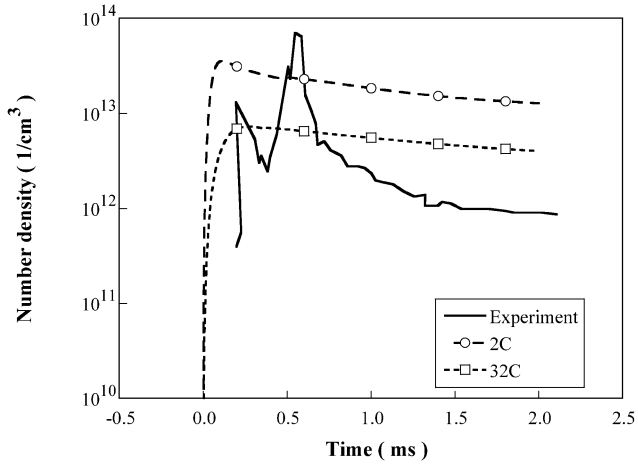

Fig. 4. Comparison of the experimental results of Kellerer et al. [33] and the modeling results of the present study for soot number density corresponding to the experimental and simulation conditions of Fig. 2.

the 2C model also results in a smaller average particle size due to the abundance of smaller particles (see Fig. 3) and more soot surface area available for surface interactions. The quantitative agreement between the model predictions for soot yield and the experimental data is improved for the smaller 2C particle size; however, this is at the expense of increased discrepancies between the 2C model and experimental results for the average soot particle diameter and the soot number density. Overall, a primary soot particle size of 32C was chosen in subsequent calculations in favor of the physical basis for this primary particle size (i.e., representing the collision of two pyrene molecules) and as a compromise between the transient soot properties under the calibration conditions.

The sensitivity of the nucleation submodel correction factor, A_C, on the quantitative agreement with the soot yield, soot number density, and soot particle-size time histories was also investigated. Increasing the correction factor increases the nucleation rate of the soot primary particles, which in turn yields an increase in the number density of soot particles and a decrease in the average particle size. Similar to the effect of changing the size of the primary soot particle, changing A_C led to a trade-off in the agreement between the experimental and the modeling results. Specifically, increasing the correction factor led to improved quantitative agreement with the soot yield, but degraded the quantitative agreement with the average particle size and number density. Based on these parametric tests, $A_C = 0.01$ was found to be an optimal compromise. Changing A_C had a minor effect on the temperature dependence of the soot model.

Fig. 5 provides the overall performance of the soot model under the calibration conditions over a wider range of temperatures. In the figure, the performance

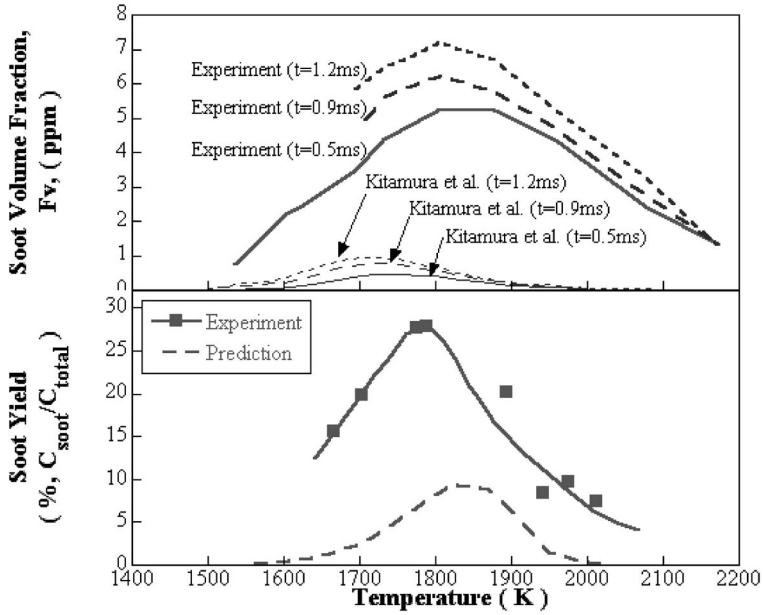

Fig. 5. Comparison of the performance of the current soot model and the soot model developed by Kitamura et al. [30]. The experimental results of Kellerer et al. [58] are shown in the upper graph. The experimental results of Kellerer et al. [33] are shown in the lower graph. (Upper graph) Benzene oxidation with $\phi = 5$, Ar = 99.5%, and $P = 3$ MPa (Fig. 8 of Kitamura et al. [30]). (Lower graph) n-Heptane oxidation with $\phi = 5$, [C] = 5.8 mol/m^3, and $P = 4$ MPa.

of the current model using the optimized parameters (i.e., $A_C = 0.01$, $A_{G3} = 3 \times 10^{12}$, and a primary particle size of 32C) is compared with the performance of the soot model developed by Kitamura et al. [30]. Note that the Kitamura model results for soot volume fraction are compared with the experimental measurements of Kellerer et al. [58] obtained from benzene oxidation shock-tube experiments. Benchmark results from the Kitamura model for soot formation from n-heptane are not available. On an absolute basis, the soot model developed in this study is in reasonable quantitative agreement with the n-heptane shock-tube studies, and the model predictions are within a factor of 5 for temperatures less than 1900 K. In contrast, the Kitamura model results differ by over an order of magnitude under some temperature conditions. Both models underpredict the soot levels relative to the experimentally determined values.

4. Model validation

Having calibrated the soot model under the benchmark conditions, the performance of the soot model for conditions outside the optimization bounds is considered next. For the following results, the soot model parameters were fixed under the optimized conditions of $A_C = 0.01$, $A_{G3} = 1 \times 10^{12}$, and a primary soot particle size of 32C. The simulation and experimental results for soot yield for a range of temperatures and pressures of 2 and 8 MPa are shown in Fig. 6. The simulations correctly reproduce the experimentally observed trend of increased soot formation with increased pressure. The temperature dependence is also well produced; however, the maximum soot yield occurs at temperatures shifted to slightly higher temperatures (by approximately 100 K) than those observed experimentally. Consistent with the results under the calibration conditions (4 MPa), the model underpredicts the soot yield. These results demonstrate that the calibrated soot model has the predictive capability to capture the soot formation characteristics of n-heptane combustion for a wide range of temperature and pressure conditions.

5. Engine simulation results

The calibrated soot model was integrated into KIVA-3V engine simulations of n-heptane combustion. The simulation conditions and engine geometry were selected to match the experimental configuration of a single-cylinder version of an International 4.5L V6 diesel engine equipped with a Siemens high-pressure common-rail injection system. Details on the engine testing facility, the KIVA input parameters, and the other submodels (such as the spray and com-

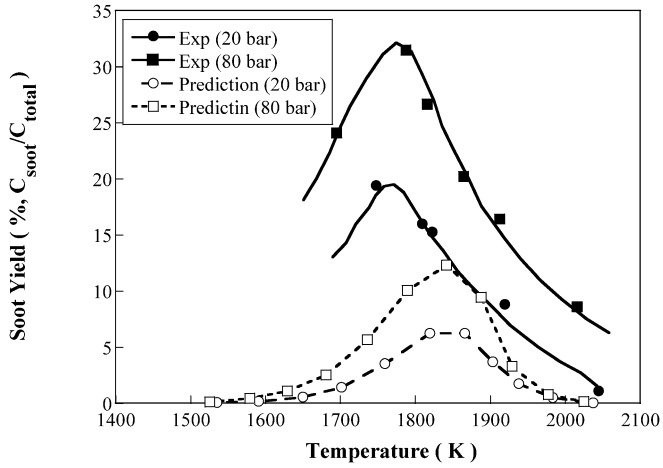

Fig. 6. Comparison of the results of the optimized soot model with the experimental results of Kellerer et al. [33] for soot yield as a function of pressure and temperature for conditions of $P = 2$ and 8 MPa, $[C] = 5.8$ mol/m^3, and $\phi = 5$.

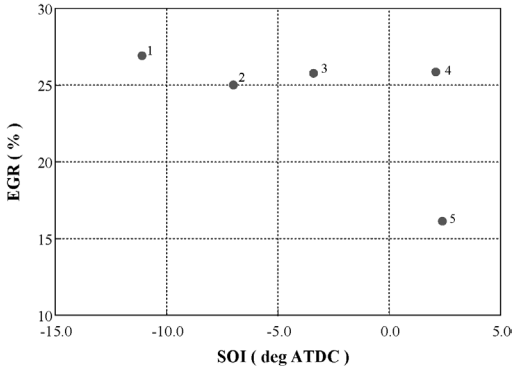

(a) Start of injection vs EGR

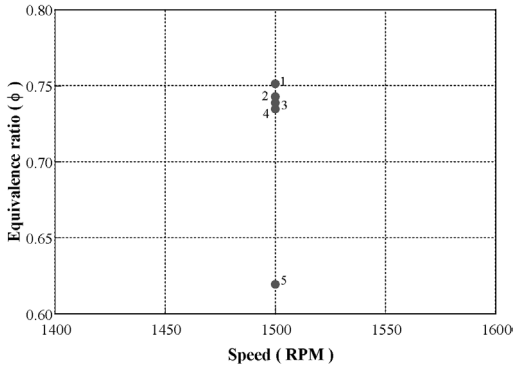

(b) Speed vs equivalence ratio

Fig. 7. Engine operating conditions considered for comparison of experimental soot measurements and numerical predictions for soot emissions. Here, the equivalence ratio is defined based on the fuel-to-air ratio in the fresh-air charge only, and does not include the effect of EGR addition.

Table 2
Engine simulation conditions

Case	SOI (° ATDC)	EGR (%, mass basis)	Speed (rpm)	ϕ[a]
1	−11.1	26.90	1500	0.75
2	−7.0	25.00	1500	0.74
3	−3.4	25.77	1500	0.74
4	2.1	25.85	1500	0.73
5	2.4	16.41	1500	0.62

[a] Here, the equivalence ratio is defined based on the fuel-to-air ratio in the fresh-air charge only and does not include the effect of EGR addition.

bustion models) are provided in Hong et al. [59–61]. The simulation conditions studied were selected based on conditions that are frequently encountered in the Federal Testing Procedure defined by the United States Environmental Protection Agency for measuring emissions for a mid-size truck [62]. The specific cases considered in terms of exhaust gas recirculation (EGR) loadings, injection timing, engine speed, and overall equivalence ratio are shown in Fig. 7 and Table 2. For this work, all simulations were conducted at the same engine speed (1500 rpm), while the EGR loading, equivalence ratio, and start of injection were varied. These engine settings include the conditions that are the highest contributors to the soot emissions

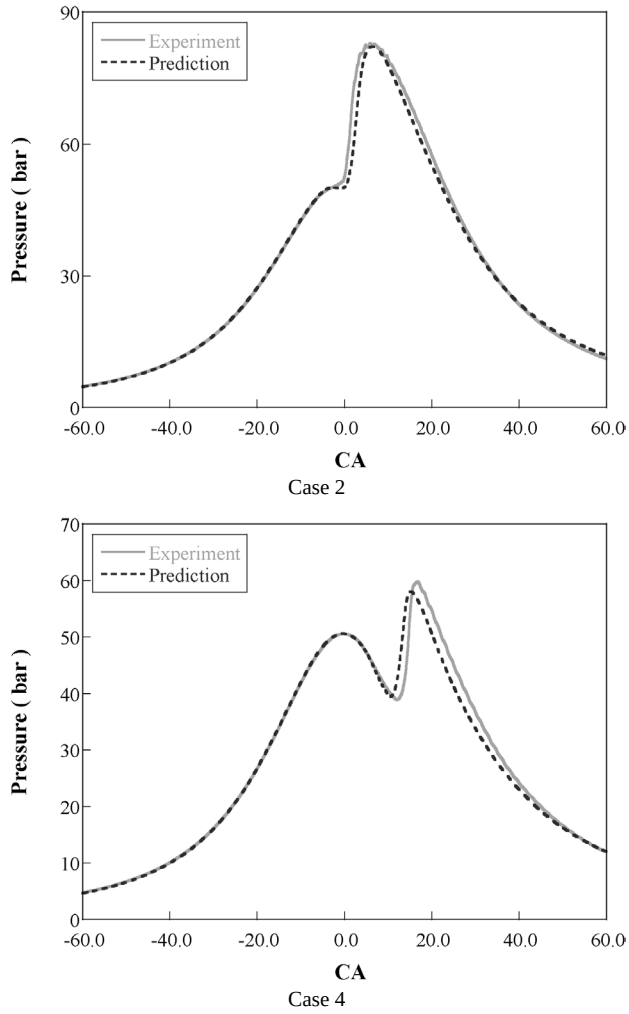

Fig. 8. Comparison of experimental and predicted results for pressure as a function of crank angle degree (CA) for Cases 2 and 4.

for the engine considered when configured in a mid-sized truck.

For the engine simulations, the diesel combustion is represented by a newly developed model which is based on a modified eddy dissipation concept (EDC). Briefly, the modified EDC model allows for more realistic representation of the thin subgrid scale reaction zone as well as the small-scale molecular mixing processes. A detailed description of the modified EDC modeling approach can be found in Hong et al. [59,61]. The soot model is directly integrated into this modified KIVA 3V program, with no changes to any of the submodel (e.g., soot, NOx, or EDC combustion) parameters. The soot calculations are made in a manner similar to the NOx emissions calculations, as a postprocessing procedure after the EDC calculations are completed at each time step.

The engine simulation results for pressure are compared with the experimental data for two representative conditions (Cases 2 and 4) in Fig. 8. The net apparent heat release rates corresponding to these conditions can be found in Hong et al. [59]. Cases 2 and 4 are indicative of operating conditions with very distinct ignition profiles due primarily to the different injection timings (−7.0° ATDC for Case 2 and 2.1° ATDC for Case 4). As seen in Fig. 8, the model predictions are in good agreement with the experimental data for both test cases. Details of the modified EDC combustion model and a comparison of measured and predicted cycle pressures and heat release rates over a wide range of conditions can be found in Hong et al. [59,61].

Fig. 9 presents simulation results for the soot volume fraction with the corresponding temperature contours and velocity vectors as a function of crank angle for conditions defined by Case 2. The simulation results for the soot number density with overlays of the O_2 contours are also provided in Fig. 9. The fuel spray

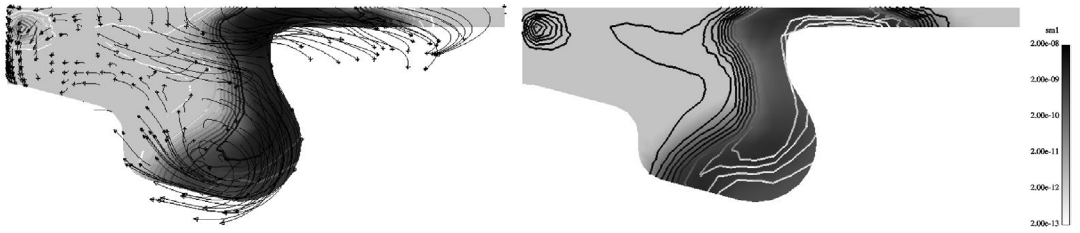

(a) 5 ATDC

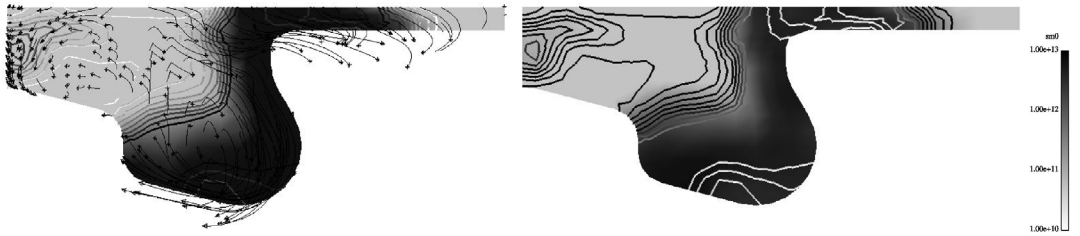

(b) 7.5 ATDC

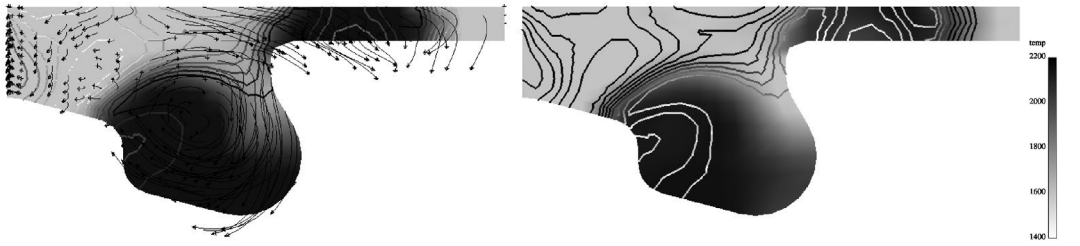

(c) 12.5 ATDC

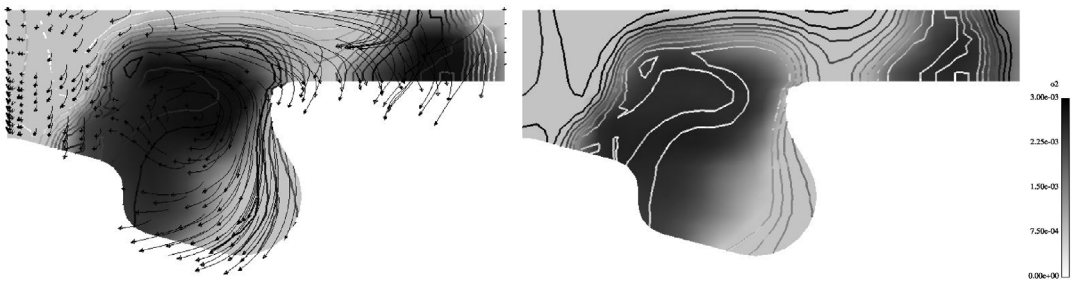

(d) 22.5 ATDC

Fig. 9. Instantaneous simulation results as a function of crank angle obtained for Case 2 operating conditions (start of injection $= -7°$ ATDC, 1500 rpm, EGR $= 25\%$, $\phi = 0.74$). The column on the left provides soot volume fraction data with temperature contour and velocity vector overlays. The column on the right provides soot number density data with O_2 contour overlays. The modeling results were obtained using the optimized input parameters. The scales provided on the far right of the figure apply to all images in Fig. 9, where sm0 = soot number density [$1/cm^3$], sm1 = soot volume fraction [dimensionless], temp = temperature [K], o2 = O_2 mass concentration [g/cm^3].

motion imparts momentum to the surrounding charge in the cylinder, while the upward movement of the piston amplifies the angular momentum of the fluid near top dead center (TDC). As seen in the figures in the left column of Fig. 9, the interaction of the two flows induces a vortex motion in the clockwise direction. The vortex flow drives the soot particles along the piston bowl surface, and the particles grow and oxidize during transport.

In addition to the clockwise vortex flow, flow toward the squish region is an important motion in the cylinder affecting the soot formation, growth, and oxidation processes. As seen in Fig. 9, as the piston moves downward, the soot cloud is divided into two

(a) 15.0 ATDC

(b) 17.5 ATDC

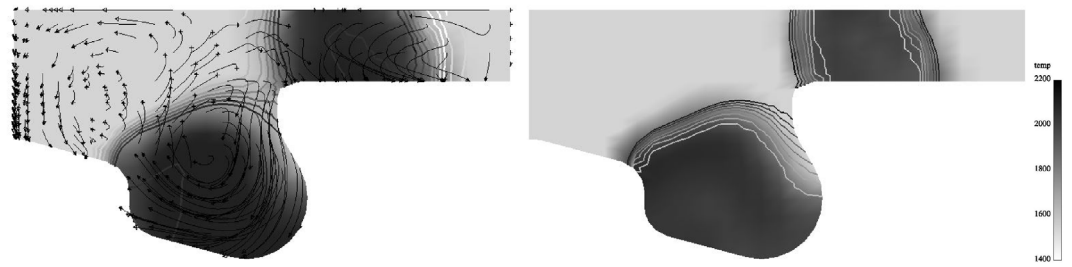

(c) 22.5 ATDC

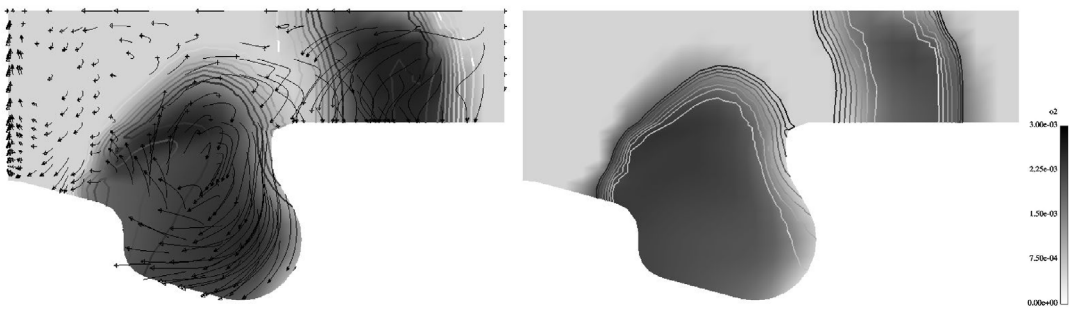

(d) 30.1 ATDC

Fig. 10. Instantaneous simulation results as a function of crank angle obtained for Case 4 operating conditions (start of injection = 2.4° ATDC, 1500 rpm, EGR = 26%, $\phi = 0.73$). The column on the left provides soot volume fraction data with temperature contour and velocity vector overlays. The column on the right provides soot number density data with O_2 contour overlays. The modeling results were obtained using the optimized input parameters. The scales provided on the far right of the figure apply to all images in Fig. 10, where sm0 = soot number density [$1/cm^3$], sm1 = soot volume fraction [dimensionless], temp = temperature [K], o2 = O_2 mass concentration [g/cm^3].

sections; one is transported by the clockwise vortex flow and the other is transported by the flow motion toward the squish region. Initially, comparable soot volume fractions are predicted in the squish and bowl regions of the cylinder. At later crank angles, however, the oxidation process is slow in the squish region and higher soot volume fractions exist in the squish region compared to the bowl region (Fig. 9d).

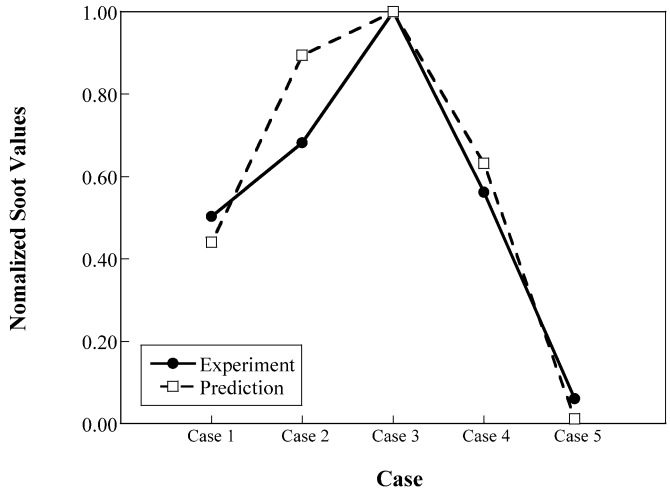

Fig. 11. Comparison of experimental and predicted soot emissions. All "experiment" data are normalized by the maximum experimental value of soot mass measured for Case 3 conditions, and all "prediction" data are normalized by the maximum predicted value for soot mass calculated for Case 3 conditions.

Fig. 10 presents simulation results for conditions corresponding to a later injection timing (Case 4) compared to the Fig. 9 simulation results (Case 2). For the late injection, high soot volume fractions are predicted at later crank angles (see Fig. 10, CA = 22.5° ATDC). The general features of the Case 4 simulation results are similar to the early injection timing results, with two regions of high soot number density affected by the vortex and squish flow motions. An important difference between the results is the smaller region of high temperatures identified in the late injection timing conditions (Figs. 10b and 10c). This is a key result, as Figs. 9 and 10 show that the high-temperature regions (shown as contour overlays) always bound the regions of high soot volume fraction. Although not shown for clarity, the OH contours also exhibit similar characteristics, i.e., high OH levels bound the regions of high soot loadings. This result is in good qualitative agreement with the experimental investigation by Dec and Tree [63], who also found that regions of high soot levels were enveloped by clouds of high OH levels.

As an indication of the computational costs associated with this comprehensive level of soot modeling, the simulation results shown in Fig. 9 required approximately 4–5 days of computational time using a Linux system, Intel Pentium 4 2.8 GHz processor with 1 GB of RAM. Thus, parametric studies can be conducted in a reasonable amount of time. In this work, the overall soot emissions (soot mass per cycle) were examined for a range of injection timings (−11–2.5° ATDC) and two exhaust gas recirculation (EGR) levels (16, 26–27%) levels. Predictions of the general combustion characteristics such as cylinder pressure and heat release agreed very well with the experimental engine data for these parametric studies (for details, see Hong et al. [59,61]).

In Fig. 11, simulation and experimental results for the particulate emissions are summarized. The experimental soot measurements are presented as normalized soot mass based on the measured AVL smoke number, where the AVL correlation for converting smoke number to soot mass concentration has been used [64]. The simulation results are in excellent agreement with the qualitative trends observed in the diesel engine study, demonstrating the predictive capability of the soot model in full-cycle engine simulations.

The results of more extensive engine simulations and comparisons with experimental data can be found in Hong et al. [61]. This work includes additional engine operating conditions and soot and NOx emission data. Explanation of observed trends for the engine studies can also be found in Hong et al. [61].

6. Conclusions

The present work is an advance in modeling soot formation within the framework of widely used engine simulations, such as KIVA-3V, using more realistic physical and chemical bases. The level of empiricism used in the model is significantly reduced from that of previous engine soot modeling studies, while simultaneously maintaining reasonable computational costs. The soot modeling approach shows good ability to reproduce the transient features observed in shock-tube time histories of rich n-heptane mixtures of soot carbon yield, particle diameter, and number density. This ability to accurately model tran-

sient soot phenomena is critical for engine simulations, as demonstrated by the crank-angle-resolved data presented in this work. The model also reproduces the experimentally observed trends for soot yield in shock-tube studies as a function of temperature and pressure. The quantitative agreement between the optimized soot model is substantially improved over the previous breakthrough work by Kitamura et al. [30], which uses a similar soot modeling approach.

Application of the soot model to engine simulation studies has been successfully demonstrated and comparisons of the computational predictions for normalized soot mass are in excellent agreement with experimentally observed trends in smoke number. The engine simulation results also confirm the critical need to accurately account for particle transport in soot modeling studies. Because the soot model is based on the fundamental phenomena important in soot formation, this model has considerable potential as a powerful new tool to lend insight into the physical and chemical mechanisms limiting soot emissions in diesel engines.

Acknowledgments

The authors sincerely thank Dr. Eric Kurtz of the Ford Motor Company for providing the engine smoke data. This work has been supported and funded through an Agreement (Simulation Based Design and Demonstration of Next Generation Advanced Diesel Technology, Contract No. DAAE07-01-3-0005) between TACOM (U.S. Army Tank-Automotive and Armaments Command), Ford Motor Company, University of Michigan, and International Truck and Engine Corporation.

References

[1] H. Hiroyasu, T. Kadota, SAE Paper 760129 (1976).
[2] G.J. Hampson, R.D. Reitz, SAE Paper 980524 (1998).
[3] A.R. Wadhwa, V. Gopalakrishnan, J. Abraham, SAE Paper 2001-01-1005 (2001).
[4] K. Nishida, H. Hiroyasu, SAE Paper 890269 (1989).
[5] P. Belardini, C. Bertoli, A. Ciajolo, A. D'Anna, N. Del Giacomo, SAE Paper 922225 (1992).
[6] M. Patterson, S.-C. Kong, G. Hampson, R.D. Reitz, SAE Paper 940523 (1994).
[7] S.-C. Kong, Z.Y. Han, R.D. Reitz, SAE Paper 950278 (1995).
[8] D.K. Mather, R.D. Reitz, SAE Paper 980789 (1998).
[9] P.A. Tesner, T.D. Snegriova, V.G. Knorre, Combust. Flame 17 (1971) 253.
[10] V.F. Surovikin, Khim. Tverd. Topliva 10 (1976) 111–122.
[11] A.A. Amsden, KIVA-3V: A Block Structured KIVA Program for Engines with Vertical or Canted Valves, Los Alamos National Lab. Report LA-13313-Ms, 1997.
[12] B.S. Haynes, H.G. Wagner, Prog. Energy Combust. Sci. 7 (1981) 229–273.
[13] J. Nagle, R.F. Strickland-Constable, in: Proc. Fifth Conference on Carbon, Pergamon Press, London, 1962, pp. 154–164.
[14] P. Belardini, C. Bertoli, N. Del Giacomo, B. Iorio, SAE Paper 932658 (1993).
[15] P. Belardini, C. Bertoli, C. Beatrice, A. D'Anna, N. Del Giacomo, Proc. Combust. Inst. 26 (1996) 2517–2524.
[16] A. Fusco, A.L. Knox-Kelecy, D.E. Foster, in: The Third International Symposium on Diagnostics and Modeling of Combustion in Internal Combustion Engines, COMODIA 94, Yokohama, Japan, 1994, pp. 571–576.
[17] A. Kazakov, D.E. Foster, SAE Paper 982463 (1998).
[18] P. Markatou, H. Wang, M. Frenklach, Combust. Flame 93 (1993) 467–482.
[19] M. Frenklach, H. Wang, in: H. Bockhorn (Ed.), Soot Formation in Combustion: Mechanisms and Models, Springer-Verlag, Heidelberg, 1994, pp. 165–189.
[20] A. Kazakov, H. Wang, M. Frenklach, Combust. Flame 100 (1995) 111–120.
[21] A. Kazakov, M. Frenklach, Combust. Flame 114 (1998) 484–501.
[22] J. Appel, H. Bockhorn, M. Frenklach, Combust. Flame 121 (2000) 122–136.
[23] F. Mauss, T. Schäfer, H. Bockhorn, Combust. Flame 99 (1994) 697–705.
[24] F. Mauss, H. Bockhorn, Z. Phys. Chem. 188 (1995) 45.
[25] F. Mauss, Ph.D. thesis, Department of Mechanical Engineering, RWTH Aachen, 1998.
[26] F. Mauss, B. Trilken, H. Breitbach, N. Peters, in: H. Bockhorn (Ed.), Soot Formation in Combustion: Mechanisms and Models, Springer-Verlag, Heidelberg, 1994, pp. 325–368.
[27] M. Fairweather, W.P. Jones, H.S. Ledin, R.P. Lindstedt, Proc. Combust. Inst. 24 (1992) 1067–1074.
[28] A. Karlsson, I. Magnusson, M. Balthasar, F. Mauss, SAE Paper 981022 (1998).
[29] H. Pitsch, H. Barths, N. Peters, SAE Paper 962057 (1996).
[30] T. Kitamura, T. Ito, J. Senda, H. Fujimoto, Int. J. Engine Res. 3 (2002) 223–248.
[31] F.X. Tanner, G.-S. Zhu, R.D. Reitz, Trans. ASME J. Eng. Gas Turbines Power 125 (2003) 534–540.
[32] M. Balthasar, F. Mauss, M. Pfitzner, A. Mack, Trans. ASME 124 (2002) 66–74.
[33] H. Kellerer, A. Muller, J. Bäuer, S. Wittig, Combust. Sci. Technol. 113–114 (1996) 67–80.
[34] S. Hong, D.N. Assanis, M.S. Wooldridge, SAE Paper 2002-01-1112 (2002).
[35] S. Hong, Ph.D. thesis, Department of Mechanical Engineering, Univ. of Michigan, Ann Arbor (2001).
[36] F. Mauss, B. Trilken, H. Breitbach, N. Peters, in: H. Bockhorn (Ed.), Soot Formation in Combustion: Mechanisms and Models, Springer-Verlag, Heidelberg, 1994.
[37] S.J. Harris, M.M. Maricq, J. Aerosol Sci. 33 (2002) 935–942.

[38] A.K.K. Virtanen, J.M. Ristimäki, K.M. Vaaraslahti, J. Keskinen, Environ. Sci. Technol. 38 (2004) 2551–2556.
[39] S. Liu, J. Hewson, J.H. Chen, H. Pitsch, Combust. Flame 137 (2004) 320–339.
[40] C. Chevalier, P. Louessard, U.C. Müller, J. Warnatz, in: Int. Symp. Diag. Modeling Combust. IC Engines, COMODIA 90, Kyoto, Japanese Society of Mechanical Engineers, 1990.
[41] H. Pitsch, N. Peters, SAE Paper 982464 (1996).
[42] M. Bollig, H. Pitsch, J.C. Hewson, K. Seshadri, Proc. Combust. Inst. 26 (1997) 729–737.
[43] D.L. Baulch, C.J. Cobos, R.A. Cox, P. Frank, G. Hayman, Th. Just, J.A. Kerr, T. Murrells, M.J. Pilling, J. Troe, R.W. Walker, J. Warnatz, J. Phys. Chem. Ref. Data 21 (1992) 411–429.
[44] D.L. Baulch, C.J. Cobos, R.A. Cox, P. Frank, G. Hayman, Th. Just, J.A. Kerr, T. Murrells, M.J. Pilling, J. Troe, R.W. Walker, J. Warnatz, Combust. Flame 98 (1994) 59–79.
[45] H.K. Ciezki, G. Adomeit, Combust. Flame 93 (1993) 421–433.
[46] R. Minetti, M. Carlier, M. Ribaucour, E. Therssen, L.R. Soche, Combust. Flame 102 (1995) 298–309.
[47] T.J. Held, A.J. Marchese, F.L. Dryer, Combust. Sci. Technol. 123 (1997) 107–146.
[48] C.V. Callahan, T.J. Held, F.L. Dryer, R. Minetti, M. Ribaucour, L.R. Sochet, T. Faravelli, P. Gaffuri, E. Ranzi, Proc. Combust. Inst. 26 (1996) 739–746.
[49] R. Seiser, H. Pitsch, K. Seshadri, W.J. Pitz, H.J. Curran, Proc. Combust. Inst. 28 (2000) 2029–2036.
[50] M. Frenklach, Phys. Chem. Chem. Phys. 4 (2002) 2028–2037.
[51] R.C. Millikan, J. Phys. Chem. 66 (1962) 794–799.
[52] K.M. Leung, R.P. Lindstedt, W.P. Jones, Combust. Flame 87 (1991) 289–305.
[53] M. Colket, R. Hall, in: H. Bockhorn (Ed.), Soot Formation in Combustion: Mechanisms and Models, Springer-Verlag, Heidelberg, 1994, pp. 442–470.
[54] K.G. Neoh, J.B. Howard, A.F. Sarofim, in: D.C. Siegla, G.W. Smith (Eds.), Particulate Carbon: Formation during Combustion, Plenum, New York, 1981, p. 261.
[55] W.C. Hinds, Aerosol Technology: Properties, Behavior, and Measurement of Airborne Particles, second ed., Wiley–Interscience, New York, 1999.
[56] K.W. Lee, H. Chen, Aerosol Sci. Technol. 3 (1984) 327–334.
[57] J.H. Seinfeld, Atmospheric Chemistry and Physics of Air Pollution, Wiley, New York, 1986.
[58] H. Kellerer, R. Koch, S. Wittig, Combust. Flame 120 (2000) 188–199.
[59] S. Hong, D.N. Assanis, M.S. Wooldridge, H.G. Im, E. Kurtz, H. Pitsch, SAE Paper 2004-01-0107 (2004).
[60] S. Hong, M.S. Wooldridge, D.N. Assanis, Proc. Combust. Inst. 29 (2002) 711–718.
[61] S. Hong, D.N. Assanis, M.S. Wooldridge, H.G. Im, E. Kurtz, submitted for publication.
[62] http://www.epa.gov/otaq/emisslab/methods/.
[63] J.E. Dec, D.R. Tree, SAE Paper 2001-01-1295 (2001).
[64] V.R. Christian, F. Knopf, A. Jaschek, W. Schindler, MTZ 54 (1993) 16–22.